




# High Performance $7 \times 8$ Ge-on-Si Arrayed Waveguide Gratings for the Midinfrared

Aditya Malik , Eric J. Stanton, *Graduate Student Member, IEEE*, Junqian Liu, Alexander Spott , *Graduate Student Member, IEEE*, and John E. Bowers , *Fellow, IEEE*

**Abstract**—Ge-on-Si low-loss waveguides and  $7 \times 8$  arrayed waveguide gratings (AWGs) are presented for operation near  $4.7 \mu\text{m}$  wavelength. Propagation loss in the range of 3 dB/cm for fully etched waveguides and 1 dB/cm for shallow-etched waveguides is reported. 200 GHz AWGs in a  $7 \times 8$  configuration with various waveguide aperture widths and etch depths are designed and characterized. For fully etched AWGs, the insertion loss values as low as  $-2.34$  and 3 dB mean cross talk of  $-29.63$  dB are achieved. The shallow-etched AWG has an insertion loss of  $-1.52$  dB and crosstalk of  $-28$  dB.

**Index Terms**—Arrayed waveguide gratings, midinfrared, planar waveguides.

## I. INTRODUCTION

THE mid-infrared wavelength range is interesting for trace gas sensing because of higher molecular absorption strength [1]. A widely tunable mid-infrared laser is desirable for sensing several trace gases using a single device which can be accomplished using photonic integrated circuits (PICs). Until now, the demonstrated integrated mid-infrared light sources are tunable in a narrow wavelength range [2]–[5]. Wavelength (de)multiplexers present an interesting way to combine multiple narrow tunable lasers in a single waveguide. AWGs fabricated on planar waveguide circuits have been used for this purpose but until recently the wavelength of operation was focused in the telecom range [6]. In the past few years there have been several demonstrations of mid-infrared AWGs based on Silicon-on-Insulator (SOI), Ge-on-Si and SiGe waveguide platforms from  $3.8 \mu\text{m}$  to  $7.6 \mu\text{m}$ . The performance of these AWGs is listed in Table I.

Recently we demonstrated beam combining of individual distributed feedback (DFB) quantum cascade lasers (QCLs) using an AWG fabricated on SOI waveguide platform [11]. While the SOI waveguide platform is established for the telecom wavelength range, a known problem with it is the high absorption of the buried silicon dioxide (BOX) layer beyond  $4 \mu\text{m}$  wavelength. The operational wavelength can be extended beyond  $4 \mu\text{m}$  by

Manuscript received February 12, 2018; revised March 20, 2018; accepted March 20, 2018. Date of publication March 26, 2018; date of current version April 10, 2018. (*Corresponding author: Aditya Malik.*)

The authors are with the Department of Electrical and Computer Engineering, University of California Santa Barbara, Santa Barbara, CA 93106 USA (e-mail: amalik@ece.ucsb.edu; estanton@ece.ucsb.edu; junqian@ucsb.edu; spott@ece.ucsb.edu; bowers@ece.ucsb.edu).

Color versions of one or more of the figures in this paper are available online at <http://ieeexplore.ieee.org>.

Digital Object Identifier 10.1109/JSTQE.2018.2819889

TABLE I  
TABLE SUMMARIZING THE PERFORMANCE OF DEMONSTRATED  
MIDINFRARED AWGS

Material System	Operational Wavelength ( $\mu\text{m}$ )	Cross Talk (dB)	Insertion Loss (dB)
SOI [7]	3.8	-23.15	-1.75
Ge-on-Si [8]	5.3	-20.00	-2.50
SiGe-on-Si [9]	4.5	-20.00	-4.00
SiGe-on-Si [10]	7.6	-20.00 (only for central channel)	-3.00
Ge-on-Si (This work, fully etched)	4.6	-28.02 (-29.63 <sup>1</sup> )	-3.24
Ge-on-Si (This work, shallow etched)	4.6	-25.42 (-28.24 <sup>1</sup> )	-1.54

<sup>1</sup> In other references, the cross talk is defined as the difference between the peak of the central channel and peak of any side lobe in all channel transmissions. The values in the brackets are calculated using a more rigorous method defined as mean 3 dB cross talk as explained later in the manuscript.

using a thick waveguide core layer, however, the high aspect ratio of the waveguides makes the fabrication process challenging. Additionally, the lasers integrated on SOI suffer from poor heat sink as the BOX layer has a low thermal conductivity. QCLs are known to have high thermal budget and hence achieving continuous wave (CW) operation at room temperatures is challenging for mid-infrared lasers integrated on SOI.

Ge-on-Si waveguide platform is emerging as a viable alternate to SOI for operation beyond  $4 \mu\text{m}$  wavelength range. The biggest advantage of Ge-on-Si as compared to some other reported waveguide platforms is that it offers a straight-forward fabrication scheme which is less prone to fabrication failures. Additionally, Ge-on-Si offers to extend the operational wavelength into long wave infrared as both silicon and germanium are widely transparent. There have been several demonstrations of devices on Ge-on-Si waveguides showing low loss waveguides from  $2.0 \mu\text{m}$  to  $8.5 \mu\text{m}$  [12], [13], [14], [15], Mach-Zehnder interferometers [14], [16], AWGs [8], planar concave gratings [17], ring resonators [18] and grating couplers [19]. A slight variation of this waveguide platform is where a graded SiGe film is grown on silicon instead of the germanium film. Several components such as low loss waveguides and AWGs are demonstrated in this waveguide platform as well [9], [10], [20].

In this paper, we present our results on low loss Ge-on-Si waveguides and AWGs. The waveguide propagation loss values are comparable to those previously reported in literature and the AWGs show superior performance as compared

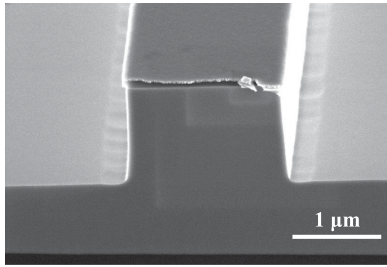


Fig. 1. SEM image of a cleaved shallow etched Ge-on-Si waveguide. The Cr hard mask is visible on the top.

to previously published mid-infrared AWGs in any waveguide platform.

## II. FABRICATION

The fabrication of Ge-on-Si waveguide circuits is done in the UCSB nanofab on 100 mm diameter wafers purchased commercially from IQE with a 2  $\mu\text{m}$  thick germanium film on (100) silicon substrate. A hard mask consisting of 100 nm PECVD  $\text{SiO}_2$  and 100 nm sputtered Cr is deposited. The wafers are exposed with desired patterns in an ASML DUV stepper following which the Cr hard mask is patterned in a Panasonic ICP system with a  $\text{Cl}_2:\text{O}_2$  plasma. The  $\text{SiO}_2$  hard mask and the germanium layer are then etched in the same system using a  $\text{CHF}_3:\text{CF}_4:\text{O}_2$  plasma. The wafers are then immersed in a HF solution for 5 minutes to undercut the  $\text{SiO}_2$  layer and lift-off the Cr hard mask. Finally, the wafers are diced and the facets are polished for edge coupling. A scanning electron microscope (SEM) image of the cleaved waveguide is shown in Fig. 1.

## III. MEASUREMENT SETUP

The measurement setup is schematically depicted in Fig. 2. Light from a commercial Daylight solutions QCL (emitting 300 mW power) is coupled in an  $\text{InF}_3$  fiber (Thorlabs) using an off axis  $90^\circ$  focusing parabolic mirror (Thorlabs) (200 mW coupled in the fiber). This fiber is connected to a set of two  $90^\circ$  off axis parabolic mirrors, which have a linear wire grid polarizer in between to select the desired polarization, to couple light in a 15  $\mu\text{m}$  wide waveguide facet. The mirrors and the wire grid polarizer are held in a cage system mounted on a piezo controlled 3-axis motion stage (Thorlabs). Coupling light in the  $\text{InF}_3$  fiber on the input side allows us to move the input motion stage independently while keeping the coupling from the QCL constant. On the output side, the light is collected using a cleaved fiber which is mounted on a similar 3-axis motion stage and has a strain gauge (Thorlabs). The connectorized end of the fiber is butt coupled to a low signal-to-noise ratio room temperature detector (Vigo) with its voltage response fed to a lock-in amplifier. The QCL is operated at a 100 KHz frequency and all the measurements are done for TM polarized light. Initially, we used a cleaved fiber for coupling into the waveguide facet (similar to the measurement scheme depicted in [8]). However it was found that the fiber was not polarization maintaining. As a result, a quarter wave plate and a half wave plate were needed to control the polarization but a large variation

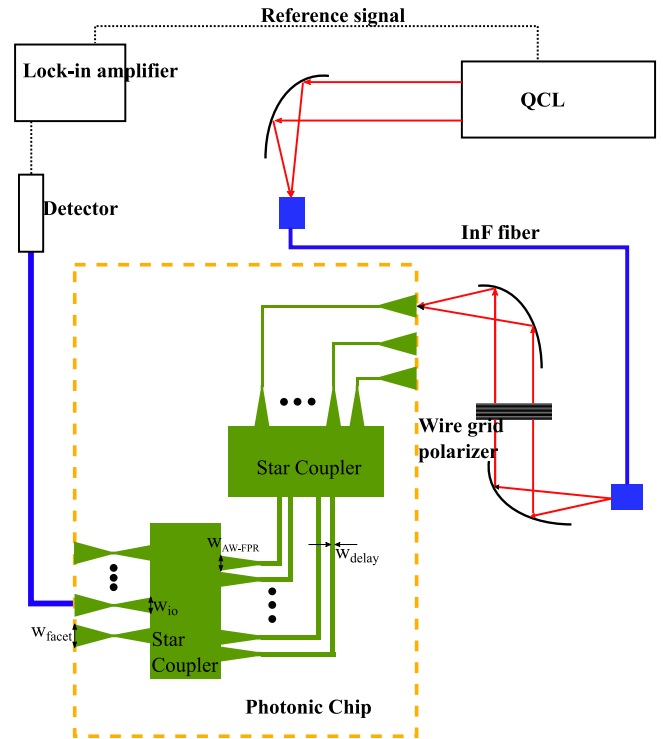


Fig. 2. Schematic diagram of the measurement setup. The schematic of the AWG shows widths of the various waveguides.

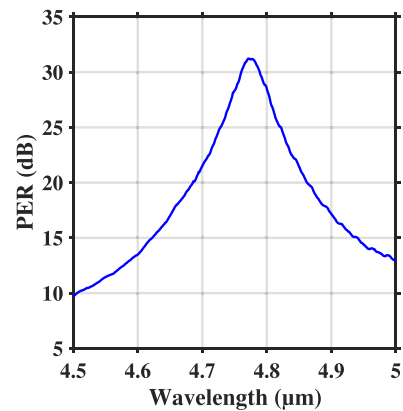


Fig. 3. Polarization extinction ratio as a function of wavelength between the TM polarized light and TE polarized light after coupling light from the QCL in the  $\text{InF}_3$  fiber and adjusting the quarter wave plate and half wave plate.

was found between the ratio of the two orthogonal polarization states as a function of wavelength, because of the relatively large length ( $\approx 2$  m) of the fiber, as shown in Fig. 3. Therefore several adjustments of the quarter wave plate and half wave plate were needed to complete a wavelength scan to characterize a device.

To achieve reliable coupling in and out of the photonic chip each time, first the input focusing mirrors and the output fiber are positioned roughly in the center of the polished waveguide facets by visually aligning the spot of a red laser coupled in the input mirror/output fiber. Then, the output fiber is moved towards the chip by translating the right y-axis piezo till the strain gauge shows a reading (which indicates that the fiber has

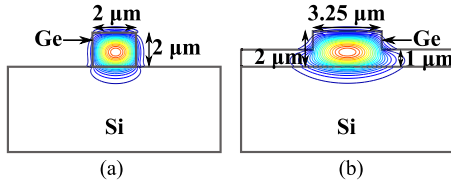


Fig. 4. 2-D contour plot of the  $E_y$  component for (a) fully etched  $2 \mu\text{m}$  wide waveguide; and (b) shallow etched  $3.25 \mu\text{m}$  wide waveguide.

hit the chip) and then backed  $10 \mu\text{m}$ . Next, both 3-axis motion stages are scanned in a  $20 \mu\text{m} \times 20 \mu\text{m}$  grid using the piezo electric controllers connected to a computer. If light is coupled to a waveguide, then the scans will show a gaussian like shape with the maxima being in the center of the waveguide. The input and output are then locked to the position of the maxima on each axis. This procedure is repeated three times. In this way, precise alignment is obtained each time minimizing errors coming from incidents such as vibrations arising from touching the stage etc.

#### IV. PROPAGATION LOSS

The two causes of the propagation loss in Ge-on-Si waveguides are the threading dislocation defects present at the silicon-germanium interface and the side wall roughness. The threading dislocation density (specified by IQE) in the grown germanium film is  $< 1e^8 \text{ cm}^{-2}$  which is comparable to previous works reported in literature [21]. Compared to fully etched waveguides, shallow etched waveguides have less side wall scattering loss. A disadvantage to the shallow etch approach is that the bend radius and hence the footprint of the devices increase.

We fabricated fully etched and shallow etched ( $1 \mu\text{m}$  etch depth) waveguides with different widths (single mode (SM) width and  $\text{SM} \pm 250 \text{ nm}$  width). The 2-D contour plot of the  $y$  component of the electric field ( $E_y$ ) for both these geometries is plotted in Fig. 4.

The propagation loss for both the waveguide geometries is calculated by the cut back method using a straight waveguide and three spirals of lengths 3 cm, 7 cm and 10 cm. The bend radius for fully etched spirals is  $100 \mu\text{m}$  and for shallow etched spirals is  $300 \mu\text{m}$ . For fully etched waveguides, the mode interacts more with the side walls for narrower widths which results in higher loss as seen in Fig. 5 and hence the propagation loss varies from 4.2 dB/cm to 2.5 dB/cm for width variation (at  $4.7 \mu\text{m}$  operation wavelength). For shallow etched waveguides, there is less overlap with the sidewalls and hence this effect is less pronounced. For shallow etched waveguides, the decrease in loss for increase in width is from 1.5 dB/cm to 1.25 dB/cm at  $4.7 \mu\text{m}$  operation wavelength. The variation in the propagation loss as a function of wavelength is a result of the fabry-perot fringes formed between the two polished waveguide facets. These fringes are not as pronounced in the shallow etched waveguides most probably because the polished facets are at an angle causing the light reflected from the facets to not couple back in the waveguide. The increase in waveguide loss for shallow etched waveguides at higher wavelengths can

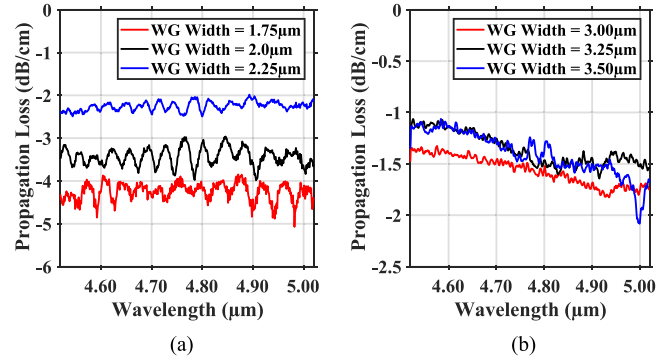


Fig. 5. Propagation loss of (a) fully etched and (b) shallow etched Ge-on-Si waveguides.

be attributed to the higher loss arising from the straight to bend section.

#### V. AWG DESIGN AND MEASUREMENTS

The AWGs presented in this paper are designed using the method described in [22]–[25]. The light from the input waveguide aperture of width  $w_{io}$  is diffracted into the input free propagation region (FPR) and is then captured by the waveguide array where each waveguide has a width of  $w_{AW-FPR}$  with pitch defined by the lithography resolution which in our case is  $w_{AW-FPR} + 200 \text{ nm}$ . The total number of the waveguides in the array is set such that 99% of the diffracted light gets captured. The waveguides in the array are then tapered to a fixed width ( $w_{\text{delay}}$ ) and their length is increased by a fixed amount. The waveguides are then tapered back gradually to a width of  $w_{AW-FPR}$  where they intersect with the output FPR to form an image on the output waveguides of width  $w_{io}$ . The width of the delay waveguides is critical as it determines the phase errors in the AWG transmission. This width is chosen such that the rate of change of the effective index ( $\frac{dn_{\text{eff}}}{dw}$ ) is minimal to minimize the deviations in the waveguide width arising from fabrication imperfections. For germanium-on-silicon waveguides, the simulated value of ( $\frac{dn_{\text{eff}}}{dw}$ ) of the  $\text{TM}_{00}$  mode for fully etched and shallow etched waveguides as a function of the waveguide width at  $4.7 \mu\text{m}$  wavelength is shown in Fig. 6. It can be observed that  $\frac{dn_{\text{eff}}}{dw}$  is inversely proportional to width. For fully etched waveguide, the delay line width was chosen to be  $4 \mu\text{m}$ . For shallow etched waveguides, there is an additional problem of cross talk between the individual waveguides and hence the delay line width was chosen to be  $5 \mu\text{m}$  to avoid any coupling. A microscopic image of a fabricated AWG is shown in Fig. 7.

Another major factor in the design of an AWG is the width of input waveguide aperture ( $w_{io}$ ) and the width of the waveguides in array at the start of the FPR ( $w_{AW-FPR}$ ). These two widths determine the Rowland radius ( $R_a$ ), the total number of waveguides ( $N_a$ ) and the difference in the length between two consecutive delay waveguides ( $\Delta L$ ).  $\Delta L$  is also dependent on the desired free spectral range (FSR). In our experiments, we decided to keep the FSR to be 200 GHz ( $\approx 15 \text{ nm}$ ) for all the designs. To study the effect of the waveguide apertures on the insertion loss and cross talk, we designed fully etched AWGs

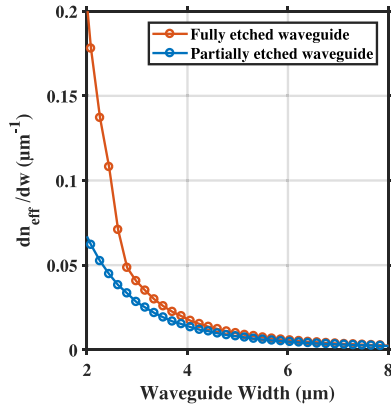


Fig. 6. Simulated variation in  $n_{\text{eff}}$  of the  $\text{TM}_{00}$  mode for fully etched and shallow etched waveguides as a function of width.

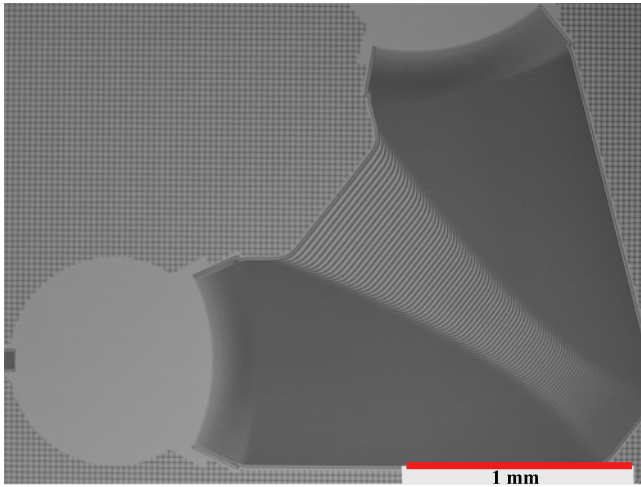


Fig. 7. Microscopic image of a fabricated AWG.

with two  $w_{io}$ ;  $5 \mu\text{m}$  (which supports the fundamental  $\text{TM}$  mode and a higher order antisymmetric  $\text{TM}$  mode) and  $7 \mu\text{m}$  (which supports higher order symmetric  $\text{TM}$  mode as well). Using our in-house simulation tool, we found that as  $w_{io}$  decreases below  $5 \mu\text{m}$ , the insertion loss increases because the angle of diffracted light from the waveguide in the star coupler increases. As  $w_{io}$  increases beyond  $7 \mu\text{m}$ , there is a chance of coupling light in the higher order  $\text{TM}$  modes and also the footprint of the AWG increases making the cross talk worse. For each input aperture width, three different  $w_{\text{AW-FPR}}$  were chosen;  $2 \mu\text{m}$ ,  $5 \mu\text{m}$  and  $7 \mu\text{m}$ . For a fixed  $w_{io}$ , the footprint of the AWG is inversely proportional to  $w_{\text{AW-FPR}}$  which would affect the cross talk. On the other hand, cross talk is also affected by coupling in the higher order modes. The above mentioned three widths of  $w_{\text{AW-FPR}}$  allow us to study how these mechanisms affect the cross talk.

The performance of an AWG is judged by the insertion loss (IL) and the cross talk. As explained in [24], the insertion loss can be calculated with better reliability using an AWG ring configuration. In our case, the available tunable QCL is not mode-hop free and can't resolve the dips of the resonance properly. As a result, we are using the conventional method of calculating the

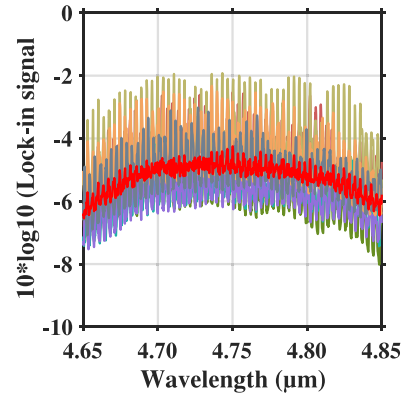


Fig. 8. Measured spectrum of 12 straight waveguides (in different colors) and the averaged spectrum (in red).

insertion loss by normalizing the AWG spectrum with respect to the averaged spectrum of the straight waveguides, obtained by measuring 12 straight waveguides as shown in Fig. 8. The uncertainty in the insertion loss using this method can be estimated by calculating the coefficient of variation [24] and is found to be 35%.

The cross talk in an AWG depends on the phase errors arising from the rough side walls and from unwanted coupling in higher order modes in the array waveguides which distort the image at the output waveguides. In our designs, the effect of the side wall phase errors is minimal because of the choice of waveguide width and the major source of noise is unwanted coupling in higher order modes. The cross talk of each channel of the AWG is calculated by using the following formula [24]

$$\text{CXT}_x = \frac{\int_{3 \text{ dB}, x} t_{a,x} d\lambda}{\int_{3 \text{ dB}, x} \left( \sum_{y=1}^{N_{ch}} t_{a,y} - t_{a,x} \right) d\lambda} \quad (1)$$

where  $t_a$  is the transmission of the channel,  $N_{ch}$  is the total number of channels and the integral is done over the 3 dB bandwidth around the peak of the channel. The mean 3 dB cross talk per channel can be defined as [24]

$$\overline{\text{XT}} = \frac{1}{N_{ch} - 1} \sum_{x=1}^{N_{ch}} \text{CXT}_x \quad (2)$$

which scales with the number of channels. On the transmission graphs, the value of  $\text{CXT}_x$  is indicated by solid squares for each channel.

#### A. $7 \mu\text{m}$ Wide Input Aperture AWGs

The transmission characteristics of the eight output channels of different AWGs with  $7 \mu\text{m}$  wide input aperture waveguide is shown in Fig. 9. The measurements were done while light was coupled to the input central channel (i.e., Channel 4). Various design parameters, the calculated insertion loss and cross talk values are given in Table II.

The mean 3 dB cross talk of the AWGs is worst for the case when  $w_{\text{AW-FPR}}$  is  $5 \mu\text{m}$  while it is best for the case when  $w_{\text{AW-FPR}}$  is  $2 \mu\text{m}$ . It can also be seen that the mean 3 dB cross talk doesn't increase with  $N_{WG}$  and the total footprint,



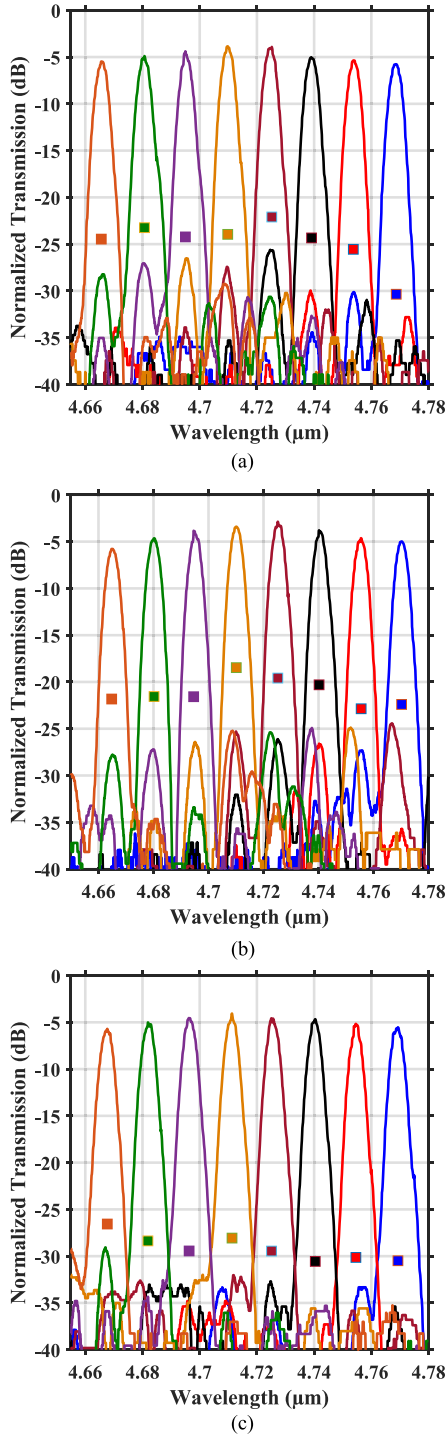


Fig. 9. Normalized transmission spectrum of the output channels of AWGs with  $7 \mu\text{m}$  wide input waveguide aperture. The width of the waveguides at start of the FPR are (a)  $7 \mu\text{m}$ , (b)  $5 \mu\text{m}$  and (c)  $2 \mu\text{m}$ . Each color represents a different channel.

TABLE II  
TABLE WITH DETAILS OF DESIGN AND MEASURED PARAMETERS OF  $7 \mu\text{m}$  WIDE INPUT APERTURE WAVEGUIDE

$w_{AW-FPR}$ ( $\mu\text{m}$ )	$N_{WG}$	$R_a$ ( $\mu\text{m}$ )	$\Delta L$ ( $\mu\text{m}$ )	IL (dB)	$\overline{XT}$ (dB)	Footprint ( $\text{mm}^2$ )
7	120	1227.51	24.52	-3.85	-24.54	9.6
5	123	912.14	23.29	-2.95	-21.17	10.6
2	151	474.79	19.62	-4.09	-25.25	16.81

TABLE III  
TABLE WITH DETAILS OF DESIGN AND MEASURED PARAMETERS OF  $5 \mu\text{m}$  WIDE INPUT APERTURE WAVEGUIDE

$w_{AW-FPR}$ ( $\mu\text{m}$ )	$N_{WG}$	$R_a$ ( $\mu\text{m}$ )	$\Delta L$ ( $\mu\text{m}$ )	IL (dB)	$\overline{XT}$ (dB)	Footprint ( $\text{mm}^2$ )
7	103	876.79	24.52	-3.48	-27.28	7.45
5	105	651.53	23.29	-2.34	-19.12	8.55
2	130	339.13	19.62	-3.24	-29.63	15.99

confirming the previously mentioned statement that the major source of cross talk is not the side wall roughness. The insertion loss is lowest for the AWG with  $w_{AW-FPR}$  of  $5 \mu\text{m}$ .

### B. $5 \mu\text{m}$ Wide Input Aperture AWG

As the width of the input aperture decreases, the total number of waveguides required in the waveguide array also decreases resulting in lower phase errors and hence cross talk. Various design and calculated parameters for the  $5 \mu\text{m}$  wide input aperture waveguides are summarized in Table III and the transmission characteristics of the eight output channels of all the AWGs for illumination of the central input channel are shown in Fig. 10.

The best performance is shown by the AWG with  $w_{AW-FPR}$  of  $2 \mu\text{m}$  with a mean 3 dB cross talk of  $-29.63$  dB. This can be attributed to the fact that a  $2 \mu\text{m}$  wide waveguide supports only a single mode. As the waveguide is tapered gradually to  $4 \mu\text{m}$  width, the coupling in the higher order modes is minimal and hence there are less phase errors. In case when  $w_{AW-FPR}$  is increased, light can get coupled to higher order modes which then cause distortion in the image at the output waveguides.

### C. Shallow Etched AWG

An AWG with shallow etched delay lines has less phase errors because of the side wall roughness in comparison to an AWG with fully etched delay lines. Additionally the reflections from the end of star coupler towards the input waveguide are minimized in a shallow etched AWG [26]. However, the total footprint of the AWG goes up as the bend radius increases. In the design of the shallow etched AWG, both the  $w_{i0}$  and  $w_{AW-FPR}$  were kept at  $8 \mu\text{m}$  width. The number of waveguides was 133 while the Rowland radius and delay line length were  $1705.95 \mu\text{m}$  and  $23.20 \mu\text{m}$  respectively. The total footprint of the AWG is  $30.8 \text{ mm}^2$ . The transmission characteristics of the output channels for central input is shown in Fig. 11 and the mean 3 dB cross talk is found to be  $-28.24$  dB while the insertion loss is  $-1.52$  dB.

### D. Noncentral Input

The AWGs presented in this work were designed in a  $7 \times 8$  configuration to be used as a  $M \times N$  wavelength (de)multiplexer. Non-central input AWGs have been used to generate flat-top response [27] and are useful in beam combining of lasers as the beam can be steered to more than one port. In case of multiple inputs, the performance of the AWG should not degrade as the input channel is changed otherwise the non-central ports can't be used. The normalized transmission of the AWGs while

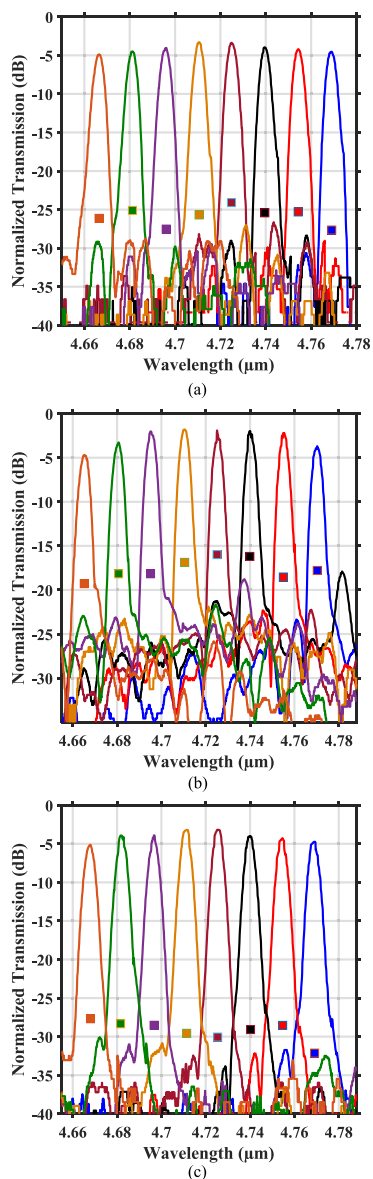


Fig. 10. Normalized transmission spectrum of the output channels of AWGs with  $5 \mu\text{m}$  wide input waveguide aperture. The width of the waveguides at start of the FPR are (a)  $7 \mu\text{m}$ , (b)  $5 \mu\text{m}$  and (c)  $2 \mu\text{m}$ . Each color represents a different channel.

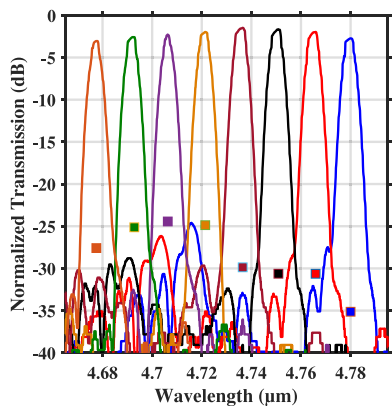


Fig. 11. Normalized transmission spectrum of the output channels of a shallow etched AWGs with  $8 \mu\text{m}$  wide input waveguide aperture. The measurements are done for illumination for central input channel.

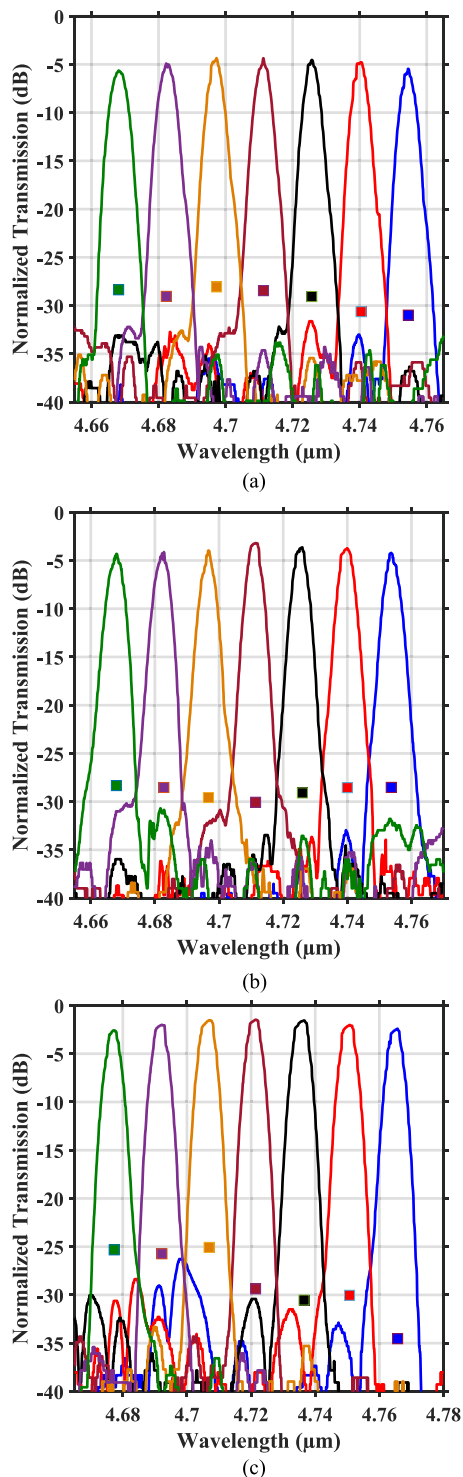


Fig. 12. Normalized transmission spectrum of the input channels when the output channel is fixed. (a)  $w_{io} 7 \mu\text{m}$ ,  $w_{AW-FPR} 2 \mu\text{m}$ , (b)  $w_{io} 5 \mu\text{m}$ ,  $w_{AW-FPR} 2 \mu\text{m}$  and (c) shallow etched AWG with both  $w_{io}$  and  $w_{AW-FPR} 8 \mu\text{m}$ . Each color represent a different input channel.

light is collected from the 5th output channel while the input channel is swept is shown in Fig. 12. It can be observed that the performance of the AWG doesn't degrade as the input channel is varied which shows the robustness of the design.

## VI. CONCLUSION

In conclusion, we have demonstrated high performance  $7 \times 8$  Ge-on-Si AWGs with 200 GHz channel spacing. For fully etched devices, the best achieved mean 3 dB cross talk is  $-29.63$  dB (corresponding insertion loss  $-3.24$  dB) and the best insertion loss is  $-2.34$  dB (corresponding mean 3 dB cross talk  $-19.12$  dB). The shallow-etched AWGs showed improvements on both accounts and the insertion loss/cross talk is found to be  $-1.52$  dB/ $-28.24$  dB. The shallow-etched AWG has a lower insertion loss as compared to a fully etched AWG at the cost of footprint. An attractive way of realizing low insertion loss and low cross talk AWG is discussed in [26] where the star coupler is partially etched and the bends are realized in fully etched waveguides. This approach requires a low loss deep to shallow waveguide transitions. It is worth mentioning that the Ge-on-Si waveguides support both the TE and TM polarized modes, and hence the designed AWG would also work for TE polarization, but the performance would not be optimal. We envisage integrating these AWGs with QCLs which emit light in TM polarization, and hence, all the characterization is carried out only for TM polarized light. QCLs are known to be power hungry devices and thus, the temperature of the AWG can change due to poor heat sinking. This will result in a shift in transmission spectrum of the AWG, however the performance is not expected to degrade. This demonstration shows that these AWGs can be used for beam combining of individual QCLs and also for wavelength (de)multiplexing applications in the mid-infrared wavelength range.

## REFERENCES

- [1] G. Roelkens *et al.*, "Silicon-based photonic integration beyond the telecommunication wavelength range," *IEEE J. Sel. Topics Quantum Electron.*, vol. 20, no. 4, pp. 394–404, Jul.–Aug. 2014.
- [2] A. Spott *et al.*, "Quantum cascade laser on silicon," *Optica*, vol. 3, no. 5, pp. 545–551, 2016.
- [3] A. Spott *et al.*, "Heterogeneously integrated distributed feedback quantum cascade lasers on silicon," *Photonics*, vol. 3, no. 4, p. 35, 2016.
- [4] A. Spott *et al.*, "Interband cascade lasers on silicon," in *Proc. IEEE Photon. Conf. Part II*, 2017, pp. 1–2.
- [5] A. Spott *et al.*, "Heterogeneous integration for mid-infrared silicon photonics," *IEEE J. Sel. Topics Quantum Electron.*, vol. 23, no. 6, Nov.–Dec. 2017, Art. no. 8200810.
- [6] S. Xiao and A. M. Weiner, "2-D wavelength demultiplexer with potential for 1000 channels in the C-band," *Opt. Express*, vol. 12, no. 13, pp. 2895–2902, 2004.
- [7] M. Muneeb *et al.*, "Demonstration of silicon-on-insulator mid-infrared spectrometers operating at 3.8  $\mu\text{m}$ ," *Opt. Express*, vol. 21, no. 10, pp. 11659–11669, 2013.
- [8] A. Malik *et al.*, "Germanium-on-Silicon mid-infrared arrayed waveguide grating multiplexers," *IEEE Photon. Technol. Lett.*, vol. 25, no. 18, pp. 1805–1808, Sep. 2013.
- [9] P. Barritault *et al.*, "Design, fabrication and characterization of an AWG at 4.5  $\mu\text{m}$ ," *Opt. Express*, vol. 23, no. 20, pp. 26168–26181, 2015.
- [10] A. Koshkinbayeva *et al.*, "Impact of non-central input in  $N \times M$  mid-IR arrayed waveguide gratings integrated on Si," *IEEE Photon. Technol. Lett.*, vol. 28, no. 20, pp. 2191–2194, Oct. 2016.
- [11] E. J. Stanton *et al.*, "Quantum cascade multispectral laser with integrated beam combiner on silicon," to be published.
- [12] Y. Chang, V. Paeder, L. Hvozدارa, J.-M. Hartmann, and H. P. Herzig, "Low-loss germanium strip waveguides on silicon for the midinfrared," *Opt. Lett.*, vol. 37, no. 14, pp. 2883–2885, 2012.
- [13] M. Nedeljkovic *et al.*, "Surface grating coupled low loss Ge-on-Si Rib waveguides and multimode interferometers," *IEEE Photon. Technol. Lett.*, vol. 27, no. 10, pp. 1040–1043, May 2015.
- [14] A. Malik *et al.*, "Germanium-on-silicon mid-infrared waveguides and Mach-Zehnder interferometers," in *Proc. IEEE Photon. Conf.*, 2013, pp. 104–105.
- [15] M. Nedeljkovic *et al.*, "Germanium-on-silicon waveguides operating at mid-infrared wavelengths up to 8.5  $\mu\text{m}$ ," *Opt. Express*, vol. 25, no. 22, pp. 27431–27441, 2017.
- [16] A. Malik *et al.*, "Ge-on-Si wavelength division multiplexing components near 4.7  $\mu\text{m}$ ," to be published.
- [17] A. Malik *et al.*, "Germanium-on-silicon planar concave grating wavelength (de)multiplexers in the midinfrared," *Appl. Phys. Lett.*, vol. 103, no. 16, 2013, Art. no. 161119.
- [18] B. Troia *et al.*, "Germanium-on-silicon vernier-effect photonic microcavities for the midinfrared," *Opt. Lett.*, vol. 41, no. 3, pp. 610–613, 2016.
- [19] S. Radosavljevic *et al.*, "Efficient 5.2  $\mu\text{m}$  wavelength fiber-to-chip grating couplers for the Ge-on-Si and Ge-on-SOI mid-infrared waveguide platform," *Opt. Express*, vol. 25, no. 16, pp. 19034–19042, 2017.
- [20] J. Ramirez *et al.*, "Low-loss Ge-rich  $\text{Si}_{0.2}\text{Ge}_{0.8}$  waveguides for mid-infrared photonics," *Opt. Lett.*, vol. 42, no. 1, pp. 105–108, 2017.
- [21] A. Malik *et al.*, "Silicon-based photonic integrated circuits for the midinfrared," *Procedia Eng.*, vol. 140, pp. 144–151, 2016.
- [22] J. F. Bauters *et al.*, "Design and characterization of arrayed waveguide gratings using ultra-low loss  $\text{Si}_3\text{N}_4$  waveguides," *Appl. Phys. A*, vol. 116, no. 2, pp. 427–432, 2014.
- [23] E. J. Stanton *et al.*, "Low-loss arrayed waveguide grating at 760 nm," *Opt. Lett.* vol. 41, no. 8, pp. 1785–1788, 2016.
- [24] E. J. Stanton *et al.*, "Low-loss demonstration and refined characterization of silicon arrayed waveguide gratings in the near-infrared," *Opt. Express*, vol. 25, no. 24, pp. 30651–30663, 2017.
- [25] E. J. Stanton *et al.*, "Silicon arrayed waveguide gratings at 2.0- $\mu\text{m}$  wavelength characterized with an on-chip resonator," *Opt. Lett.*, vol. 43, no. 5, pp. 1135–1138, 2018.
- [26] W. Bogaerts *et al.*, "Silicon-on-insulator spectral filters fabricated with CMOS technology," *IEEE J. Sel. Topics Quantum Electron.*, vol. 16, no. 1, pp. 33–44, Jan.–Feb. 2010.
- [27] K. Maru *et al.*, "Demonstration of flat-passband multi/demultiplexer using multi-input arrayed waveguide grating combined with cascaded Mach-Zehnder interferometers," *J. Lightw. Technol.*, vol. 25, no. 8, pp. 2187–2197, 2007.



**Aditya Malik** received the Bachelors degree from Delhi University, New Delhi, India, in physics following which he joined the Indian Institute of Technology Delhi, New Delhi, India for an M.Sc. program in physics.

He was a DAAD Fellow with FU Berlin during his Master studies. From October 2010 to March 2015. He received the Ph.D. degree from the Photonics Research Group, Ghent University, Ghent, Belgium, where he developed a novel CMOS-compatible waveguide platform beyond the telecommunication wavelength range. After completion of the Ph.D. degree, he worked on various topics, e.g., realizing integrated gas sensors, external cavity tunable lasers, and wavelength demultiplexers operating in midinfrared. His current research interest focuses on integration of midinfrared light sources on CMOS-compatible passive waveguide platforms. He has authored or co-authored more than 30 journals and conference papers, which have been cited more than 500 times.



**Eric J. Stanton** (S'08–GS'13) received the B.S. degree in electrical engineering from California Polytechnic State University San Luis Obispo, San Luis Obispo, CA, USA, in 2012, and the M.S. degree in electrical and computer engineering from the University of California, Santa Barbara, CA, USA, in 2014, where he is currently working toward the Ph.D. degree with emphasis on photonics, focusing on devices for multioctave spectral combining of heterogeneously integrated lasers on silicon.



**Junqian Liu** received the B.S. degree in electrical engineering from the University of California, Santa Barbara, CA, USA, in 2017, and is currently working toward the M.S. degree in materials engineering at the same university.



**Alexander Spott** (S'10–GS'17) received the B.S. degree in physics from the University of Washington, Seattle, WA, USA, in 2011, and the M.S. degree in electrical and computer engineering from the University of California, Santa Barbara, CA, USA, in 2015, where he is currently working toward the Ph.D. degree.

His research interests include midinfrared optoelectronics and silicon photonic integration. He has authored or co-authored more than 30 journals and conference papers, which have been cited more than

400 times. He was the recipient of a National Science Foundation Graduate Research Fellowship in 2012.



**John E. Bowers** (F'94) received the M.S. and Ph.D. degrees from Stanford University, Stanford, CA, USA.

He holds the Fred Kavli Chair in nanotechnology, and is the Director of the Institute for Energy Efficiency and a Professor with the Departments of Materials and Electrical and Computer Engineering, University of California, Santa Barbara (UCSB), CA, USA. He is a Cofounder of Aurrion, Aerius Photonics, and Calient Networks. He was with the AT&T Bell Laboratories and Honeywell before joining the UCSB. He has authored or co-authored eight book chapters, 700 journal papers, 900 conference papers, and is the recipient of 64 patents. He was the recipient of the IEEE Photonics Award, the OSA Tyndal Award, the OSA Holonyak Prize, the IEEE LEOS William Streifer Award, and the South Coast Business and Technology Entrepreneur of the Year Award. He and his coworkers were the recipient of the EE Times Annual Creativity in Electronics Award for most promising technology for the hybrid silicon laser in 2007. He is a Member of the National Academy of Engineering and the National Academy of Inventors. He is a Fellow of the OSA and the American Physical Society.